Volume 13 | Number 10 | 19 May 2026

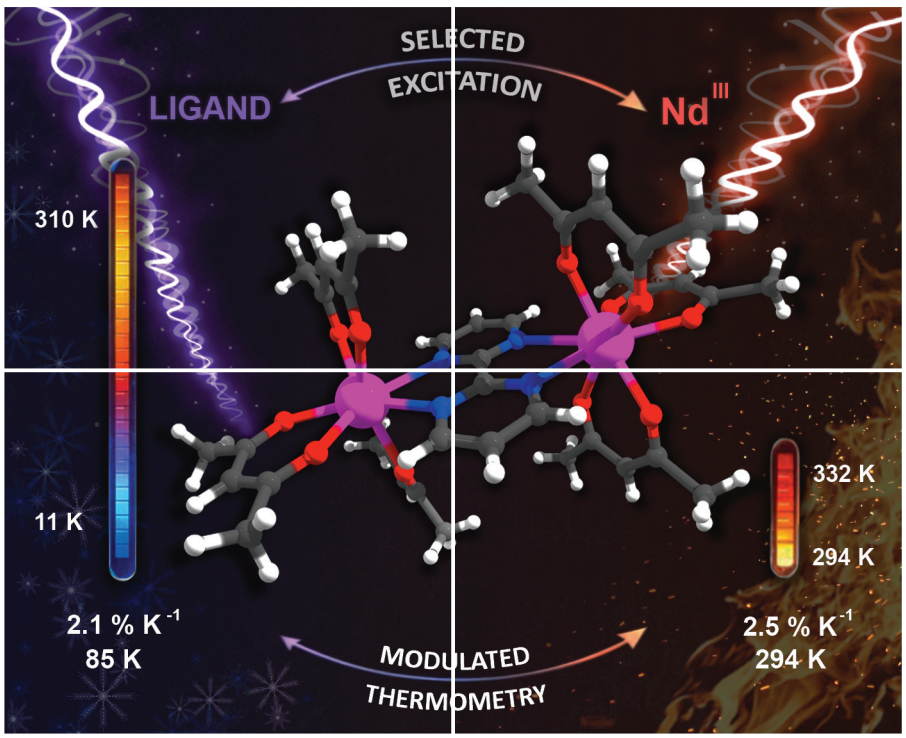

INORGANIC CHEMISTRY

FRONTIERS

CCS 中国化学会 CHINESE CHEMICAL SOCIETY
PEKING UNIVERSITY 1898
ROYAL SOCIETY OF CHEMISTRY
rsc.li/frontiers-inorganic

INORGANIC CHEMISTRY FRONTIERS

RESEARCH ARTICLE

Published on 09 March 2026
Licence and permissions

Cite this: *Inorg. Chem. Front.*, 2026, **13**, 4229

Tunable Nd^{3+} dimer luminescent molecular thermometer *via* Stark sublevels

Yolimar Gil, *[a] Julio Corredoira-Vázquez, [b,c] Ricardo Costa de Santana, [d] Carlos D. S. Brites, [e] Luís D. Carlos, [e] Evgenia Spodine, [a] Daniel Aravena [f] and Pablo Fuentealba [a]

Received 9th December 2025,
Accepted 7th March 2026

DOI: 10.1039/d5qi02484f

rsc.li/frontiers-inorganic

The near-infrared (NIR) luminescence thermometry performance of the Nd-based dimer {[Nd(acac)$_3$]$_2$(μ-bpm)} (**Nd$_2$**) (where acac$^-$ denotes acetylacetonate and bpm is 2,2′-bipyrimidine) was investigated under both ligand- and metal-centered excitation. To resolve the Stark components of the $^4F_{3/2} \rightarrow {}^4I_{11/2}$ transition, *ab initio* electronic structure calculations were performed. The opposite temperature dependences of the lower- and higher-energy components of the $^4F_{3/2}$ level were used as a thermometric parameter, expressed through the luminescence intensity ratio (LIR). Under ligand-centered excitation at 370 nm, **Nd$_2$** exhibited a maximum relative sensitivity (S_m) of 2.1% K^{-1} at 85 K, across the 85–285 K range, demonstrating excellent thermal performance at low temperatures. Considering the relevance of NIR-to-NIR emitters for biomedical applications, the thermometric response was also evaluated under metal-centered excitation at 804 nm within the physiological range (294–332 K). In this case, an unprecedented S_m value of 2.5% K^{-1} at 294 K was obtained, setting a new benchmark for Nd-based molecular thermometers and highlighting its potential for biological temperature sensing. Overall, **Nd$_2$** operates as a versatile luminescent molecular thermometer whose thermal response can be tuned simply by selecting the excitation wavelength (UV or NIR), enabling adaptable, application-specific thermometric behavior.

Introduction

Trivalent lanthanide ions (Ln^{3+}) that emit in the near-infrared (NIR) region have attracted significant research interest due to their applications in optical telecommunications,[1,2] lasers[3,4] and light-emitting devices,[5,6] as well as in biomedical contexts.[7–10] In particular, Ln^{3+} ions that both absorb and emit in the NIR region (known as NIR-to-NIR emitters) have been extensively investigated for bioimaging, biosensing, and luminescence ratiometric thermometry.[11–14] These applications exploit the deeper tissue penetration of NIR radiation within the so-called biological windows (BWs; 700–950 nm (I), 1000–1350 (II), and 1550–1870 nm (III)). Moreover, NIR excitation minimizes tissue autofluorescence and enhances image contrast.[12,15,16]

Among lanthanides, the neodymium ion (Nd^{3+}) is a promising candidate for *in vivo* luminescence thermometry. Direct excitation of the $^4I_{9/2} \rightarrow {}^4F_{5/2} + {}^2H_{9/2}$ transition, around 804 nm (BW-I), produces NIR emission bands spanning both BW-I and BW-II.[13,17] Nd^{3+} offers an additional advantage for temperature sensing due to the presence of thermally coupled levels (TCLs), such as the $^4F_{7/2}/{}^4F_{5/2}$ and $^4F_{5/2}/{}^4F_{3/2}$ excited states. Typically, the luminescence intensity ratio (LIR) of transitions originating from these TCLs is employed to evaluate the thermometric performance of Nd-based systems.[18] Since the Nd^{3+} emission bands within BW-I and BW-II arise from the $^4F_{3/2}$ level, which splits into two Stark sublevels, most Nd^{3+}-based luminescent thermometers rely on the LIR between transitions derived from these components.[19]

While initial studies concentrated on nanoparticles,[13,19–22] recent attention has broadened to include the thermometric properties of lanthanide complexes,[18,23–27] inorganic phosphors, and ceramic materials.[28,29] These molecular luminescent thermometers offer a distinct advantage: their luminescence can be sensitized through coordination with suitable organic ligands,[30,31] enabling NIR emission under both ligand- and metal-centered excitation and thereby broadening their potential applications. Furthermore, the crystal field

[a]*Facultad de Ciencias Químicas y Farmacéuticas, Universidad de Chile, Olivos 1007, 8380544 Santiago, Chile. E-mail: yolimar.gil@ciq.uchile.cl*
[b]*Departamento de Química Inorgánica, Facultade de Química, Universidade de Santiago de Compostela, 15782 Santiago de Compostela, Spain*
[c]*Institute of Materials (iMATUS), Universidade de Santiago de Compostela, 15782 Santiago de Compostela, Spain*
[d]*Instituto de Física, Universidade Federal de Goiás, Campus Samambaia, 74690-900 Goiânia, GO, Brazil*
[e]*Phantom-g, CICECO – Aveiro Institute of Materials, Department of Physics, University of Aveiro, 3810-193 – Aveiro, Portugal*
[f]*Facultad de Química y Biología, Universidad de Santiago de Chile, Casilla 40, Correo 33, Santiago, Chile*

imposed by the coordinated ligands plays a crucial role in Stark splitting and in defining the energy gap between TCLs, both of which directly influence the LIR and thermometric performance. For Nd^{3+}-based coordination compounds, luminescence thermometry has thus far been conducted using either ligand[25]- or metal-centered[24] excitation. However, to the best of our knowledge, both excitation pathways have not yet been explored in the same Nd^{3+} complex.

Here, we investigate the luminescence thermometry of the {[Nd(acac)$_3$]$_2$(μ-bpm)} complex (**Nd$_2$**), where acac$^-$ denotes acetylacetonate and bpm is 2,2′-bipyrimidine, under both indirect (ligand-centered) and direct (metal-centered) excitation. The thermometric parameter is the LIR between two Stark components of the $^4F_{3/2} \rightarrow {}^4I_{11/2}$ transition. Our results demonstrate that the excitation pathway modulates the thermal response by altering the population dynamics of the $^4F_{3/2}$ emissive level. Notably, this study provides the first demonstration of Nd-based luminescent thermometers operating under both excitation modes, while also achieving competitive relative thermal sensitivity (S_r) values, thereby extending their potential beyond biomedical sensing to broader photonic and temperature-mapping applications.

Experimental

Reagent-grade chemicals and HPLC-quality solvents were used as received. The synthesis of **Nd$_2$** was performed following a reported procedure with some modifications[32] (see SI). The microwave-assisted synthesis was executed with an Anton Paar microwave reactor, MonoWave 200.

Physical measurements

Fourier transform infrared (FTIR) spectra were recorded on a SpectrumTwo spectrophotometer from PerkinElmer, equipped with an attenuated total reflectance (ATR) accessory from PIKE Instruments. Thermogravimetric analysis (TGA) was performed using an Iris TG209 analyzer from Netzsch. Data were collected from room temperature to 870 K by using a 10 K min^{-1} heating rate in nitrogen atmosphere. The crystal structure of **Nd$_2$** was determined by single-crystal X-ray diffraction (XRD). A complete dataset was collected on a SMART-APEX II CCD diffractometer at room temperature. Data reduction was performed using SAINT,[33] and the structure was solved by the Patterson heavy atom method, followed by completion through Difference Fourier Synthesis and refinement by least-squares using SHELXL.[34,35] Multi-scan or numerical absorption corrections were applied using SADABS.[35] Powder X-ray diffraction (PXRD) patterns were collected at room temperature using a Bruker D-8 ADVANCE equipment, with Cu$K_{\alpha1}$ radiation.

The emission and excitation spectra (solid-state) were recorded on a modular double grating excitation spectrofluorimeter (Fluorolog-3, Horiba Scientific) with a TRIAX 320 emission monochromator coupled to a H9170 Hamamatsu photomultiplier for the detection in the near infrared spectral range. The excitation sources were a 450 W Xe arc lamp and a 804 nm diode laser (Crystal Laser LC) operating at 175 mW, which was focused onto a spot area of 0.16 cm^2. The emission spectra were corrected for detection and the optical spectral response of the spectrofluorimeter, while the excitation spectra were corrected for the spectral distribution of the lamp intensity using a photodiode reference detector. The temperature was controlled with a helium-closed cycle cryostat, a vacuum system (4 × 10^{-4} Pa), and an auto-tuning temperature controller (Lakeshore 330) with a resistance heater.

Electronic structure calculations

All calculations were performed as implemented in the ORCA 5.0.4 software package.[36,37] CASSCF(3,7) calculations[38] considered the 4f shell of the Nd^{3+} ion as the active space and were set to calculate 35 quartet and 112 doublet roots. The basis set was SARC2-DKH-QZVP for Nd[39] and the relativistically recontracted version of Def2-TZVP[40] for light elements. Scalar relativistic and spin–orbit effects were described by the DKH2 Hamiltonian[41] and the quasidegenerate perturbation theory (QDPT), respectively. To produce the emission spectrum, CASSCF energies were corrected according to the method described elsewhere.[42]

The multireference CASSCF + QDPT approach employed here explicitly incorporates both scalar relativistic effects and spin–orbit coupling, which is essential for an accurate description of the electronic structure and Stark splitting of lanthanide systems.

Results and discussion

Structural characterization

The FTIR spectrum of **Nd$_2$** (Fig. S1) shows a strong asymmetric doublet at 1581 and 1564 cm^{-1}, corresponding to the ring-stretching vibrations of the bpm ligand. This feature is characteristic of the bis-chelating μ-bpm bridging mode reported previously.[43,44] Single-crystal XRD data confirm this coordination mode and show that **Nd$_2$** crystallizes in the triclinic $P\bar{1}$ space group (Table S1). As illustrated in Fig. 1, the structure consists of two octacoordinated Nd^{3+} centers bridged by a bpm

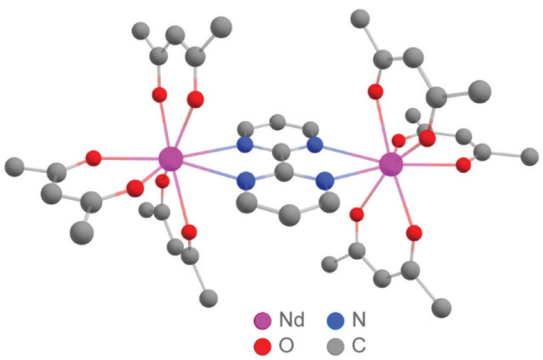

Fig. 1 Molecular structure for **Nd$_2$**. The hydrogen atoms are omitted for clarity.

ligand. Each metal ion is coordinated by six oxygen atoms from three bidentate $acac^-$ ligands, with the remaining two sites occupied by nitrogen atoms from bpm. PXRD further confirms the phase purity of the bulk sample and its concordance with the single-crystal structure (Fig. S2), matching the previously reported pattern[32] (Fig. S2).

TGA confirms the absence of water molecules or solvent outside the coordination sphere of **Nd_2**. The complex remains stable up to 220 °C (Fig. S3), a level of thermostability that supports its application in luminescence thermometry across the temperature range investigated in this study.

Photoluminescence studies

Fig. 2a shows the excitation and emission spectra of **Nd_2** at room temperature. The excitation spectrum displays two broad bands centered at 272 and 370 nm, assigned to the $\pi \rightarrow \pi^*$ electronic transitions of the bpm and $acac^-$ ligands, respectively.[45] Above 420 nm, sharp peaks corresponding to Nd^{3+} 4f–4f transitions are observed. The stronger absorption intensity of the $acac^-$ ligand relative to bpm indicates that the β-diketonate ligand acts as the more efficient antenna for sensitizing Nd^{3+} NIR luminescence. In addition, the intense band at 804 nm, corresponding to the Nd^{3+} $^4I_{9/2} \rightarrow {}^4F_{5/2} + {}^2H_{9/2}$ transitions, suggests that metal-centered excitation at this wavelength should effectively generate efficient NIR luminescence. Accordingly, two excitation wavelengths were selected to record the NIR emission spectra of **Nd_2**, 370 and 804 nm.

Under 370 nm excitation, two NIR emission bands centered at ~1060 and 1335 nm were observed, corresponding to the $^4F_{3/2} \rightarrow {}^4I_{11/2}$, $^4I_{13/2}$, respectively (Fig. 2b). Upon excitation at 804 nm, the same two bands were detected, together with an additional band at 894 nm, assigned to the $^4F_{3/2} \rightarrow {}^4I_{9/2}$ transition. The $^4F_{3/2} \rightarrow {}^4I_{11/2}$ transition appears as a well-structured band comprising five peaks at 1047.0, 1060.0, 1070.0, 1082.5, and 1089.0 nm (Fig. 2b). These peaks correspond to transitions between the Stark components of the $^4F_{3/2}$ and $^4I_{11/2}$ levels. Notably, this transition can theoretically include up to twelve Stark components.[42]

Ab initio calculations

To assign the Stark components associated with the observed peaks, *ab initio* electronic structure calculations were carried out. Following a recently reported protocol,[42] the simulated emission spectrum of **Nd_2** was generated (Fig. S4). The calculated wavelengths, shape, and relative intensities for the $^4F_{3/2} \rightarrow {}^4I_{11/2}$ and $^4F_{3/2} \rightarrow {}^4I_{13/2}$ transitions show good agreement with the experimental data. The most intense transition ($^4F_{3/2} \rightarrow {}^4I_{11/2}$) was further decomposed into contributions arising from the individual Stark components of $^4F_{3/2}$ and $^4I_{11/2}$ levels. This decomposition, together with a simplified energy-level diagram, is presented in Fig. 3. Given that the $^4F_{3/2}$ splits into two Kramers doublets and the $^4I_{11/2}$ level into six, up to twelve transitions are expected. Transitions originating from the lower-energy Stark component of the $^4F_{3/2}$ level (denoted Y_1) to the six $^4I_{11/2}$ components (Z_1–Z_6) are shown in blue, whereas those originating from the higher-energy component (Y_2) are depicted in red.

As shown in Fig. 3a, the calculated spectrum reproduces a five-peak pattern, in good agreement with the experimental

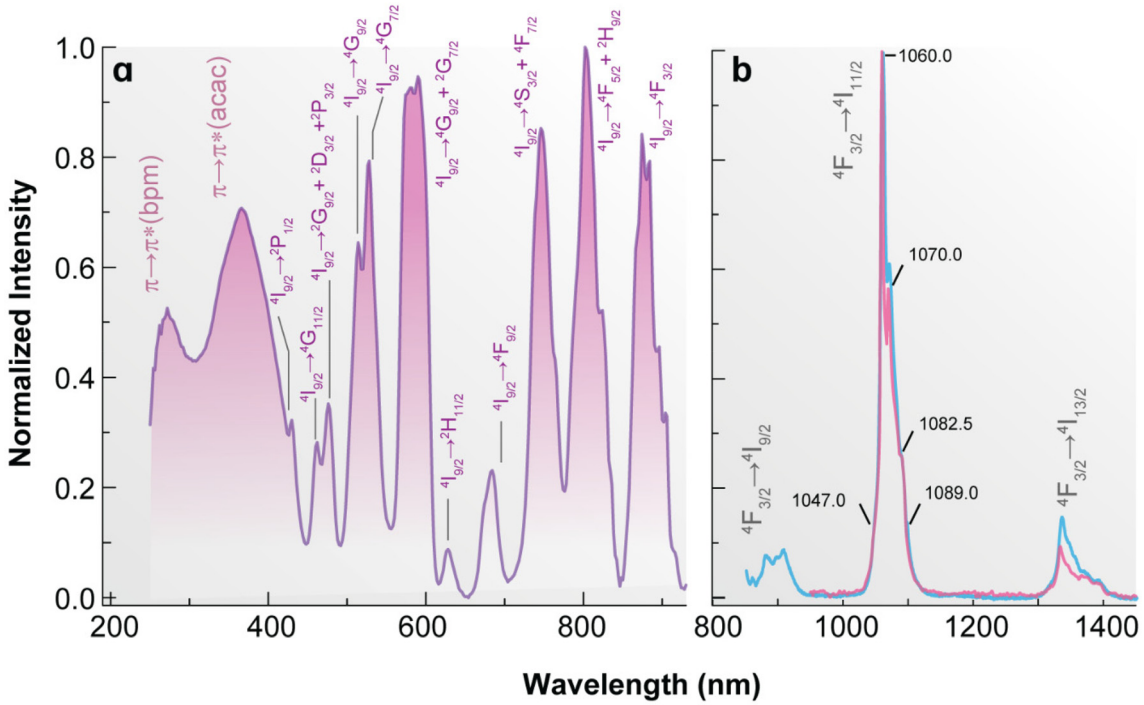

Fig. 2 Room temperature (a) excitation and (b) emission spectra of **Nd_2**. In (a), the monitoring wavelength is 1060 nm (at the $^4F_{3/2} \rightarrow {}^4I_{11/2}$ transition), while in (b) the excitation wavelengths are 370 nm (purple) and 804 nm (blue).

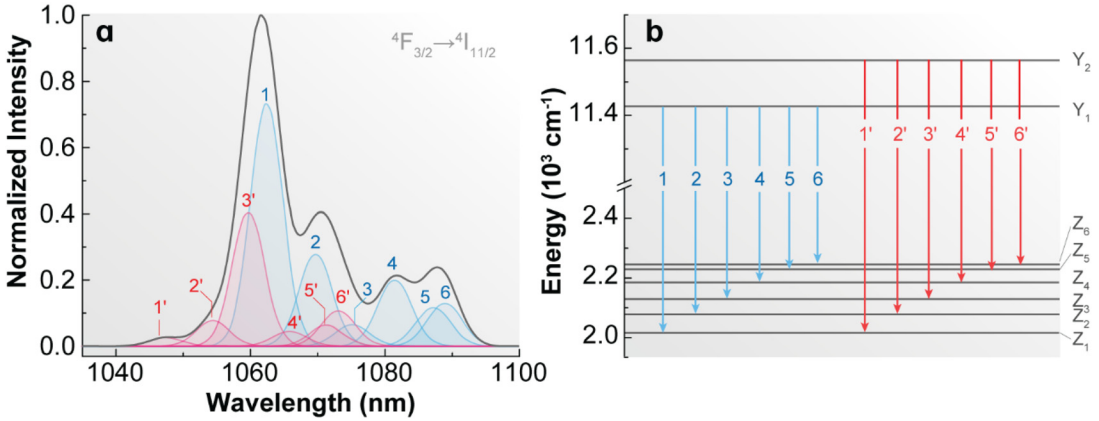

Fig. 3 (a) Decomposition of the $^4F_{3/2} \rightarrow {}^4I_{11/2}$ transition of **Nd_2** into the corresponding Stark components. Blue and red bands indicate transitions originating from the lower-energy (Y_1) and higher-energy (Y_2) Stark components of the $^4F_{3/2}$ level, respectively. The black line is the sum of all contributions (b) Calculated energy-level diagram of **Nd_2**.

emission profile (Fig. 2b). According to the energy-level diagram depicted in Fig. 3b, the weak band at 1047.0 nm arises from the $Y_2 \rightarrow Z_1$ transition. Because this transition involves the Y_2 level, the corresponding band (denoted 1′) is classified as a hot band. The next two peaks, centered at 1060.0 nm and 1070.0 nm, are assigned to the $Y_1 \rightarrow Z_1$ (1) and $Y_1 \rightarrow Z_2$ (2) transitions, respectively. The 1060.0 peak also includes contributions from the hot-band transitions $Y_2 \rightarrow Z_{2-4}$ (2′, 3′, and 4′). Similarly, the 1070.0 nm peak contains contributions from the hot-band transitions $Y_2 \rightarrow Z_{5,6}$ (5′ and 6′). The remaining two peaks, at 1082.0 nm and 1089.0 nm, are attributed to the $Y_1 \rightarrow Z_4$ (4) and $Y_1 \rightarrow Z_{5-6}$ (5 and 6) transitions, respectively.

The calculated energy gap between Y_2 and Y_1 Stark components is small (ΔE = 135.2 cm^{-1}, Fig. 3b). As a result, Y_2 can be thermally populated from Y_1 as the temperature increases. Consequently, transitions originating from Y_2 (hot bands) are expected to display pronounced temperature dependence. This thermally activated redistribution of population between Y_1 and Y_2 provides the fundamental mechanism underlying the thermometric response of **Nd_2**.

Temperature-dependent photoluminescence and thermometry

Fig. 4a presents the temperature-dependent NIR emission spectra of **Nd_2** recorded under 370 nm excitation over the 11–310 K range. At low temperatures, the $^4F_{3/2} \rightarrow {}^4I_{11/2}$ and $^4F_{3/2} \rightarrow {}^4I_{13/2}$ transitions exhibit well-resolved Stark splitting. As temperature increases, the intensity of both transitions progressively decreases. An enlarged view of the $^4F_{3/2} \rightarrow {}^4I_{11/2}$ transition (Fig. 4b) reveals, in addition to the five peaks previously identified (Fig. 2b), a sixth feature at 1074.5 nm that becomes clearly discernible at low temperatures. Although this transition can theoretically involve up to twelve Stark components, spectral overlap prevents full experimental resolution. To ensure reliable spectral deconvolution, the 11 K spectrum (where thermal broadening is minimal) was used to determine the peak energies. The band was modeled using six Lorentzian components centered at 1047.0, 1060.0, 1070.0, 1074.5, 1082.5, and 1091.0 nm (see SI). These peaks represent the most distinguishable spectral features and provide an accurate representation of the band profile while avoiding overparametrization.

As shown in Fig. 4b, the overall emission intensity decreases with increasing temperature, except for the peaks at 1047.0 and 1074.5 nm, which exhibit clear intensity enhancement. This trend is more evident in the evolution of their integrated areas (Fig. S5). These two peaks are therefore assigned as hot bands originating from the upper Stark component (Y_2) of the $^4F_{3/2}$ level. This assignment is consistent with the spectral decomposition of the $^4F_{3/2} \rightarrow {}^4I_{11/2}$ band (Fig. 3), where the 1047.0 nm peak corresponds to the $Y_2 \rightarrow Z_1$ (1′) transition. The 1074.5 nm band exhibits more complex behavior due to spectral overlap between the hot-band transitions $Y_2 \rightarrow Z_{5-6}$ (5′ and 6′) and the $Y_1 \rightarrow Z_3$ (3) transition. At low temperature, the $Y_1 \rightarrow Z_3$ contribution dominates. As temperature increases, thermal population of Y_2 enhances transitions 5′ and 6′, while the $Y_1 \rightarrow Z_3$ contribution diminishes. The net increase in the integrated intensity of the 1074.5 nm peak confirms that the growth of the hot-band contributions exceeds the reduction of the Y_1-derived component. The 1091.0 nm peak displays a broader profile due to comparable contributions from $Y_1 \rightarrow Z_5$ and $Y_1 \rightarrow Z_6$ transitions. For clarity, each of the six peaks was assigned according to its dominant Stark component contribution (inset of Fig. 4b), although overlapping contributions were considered in the quantitative analysis.

To assess thermometric performance under ligand-centered excitation, the thermometric parameter Δ_L was defined as the ratio between the integrated intensities of the hot bands (1047.0 and 1074.5 nm) and those originating from the Y_1 Stark component (1060.0, 1082.5, and 1091.0 nm). The peak at 1070.0 was disregarded due to the strong spectral overlap between transitions 3 and 5′, 6′. The Boltzmann behavior was verified by plotting $\ln(\Delta_L)$ as a function of $1/T$ (Fig. 4c), yielding a linear dependence over 85–285 K. This demonstrates thermal

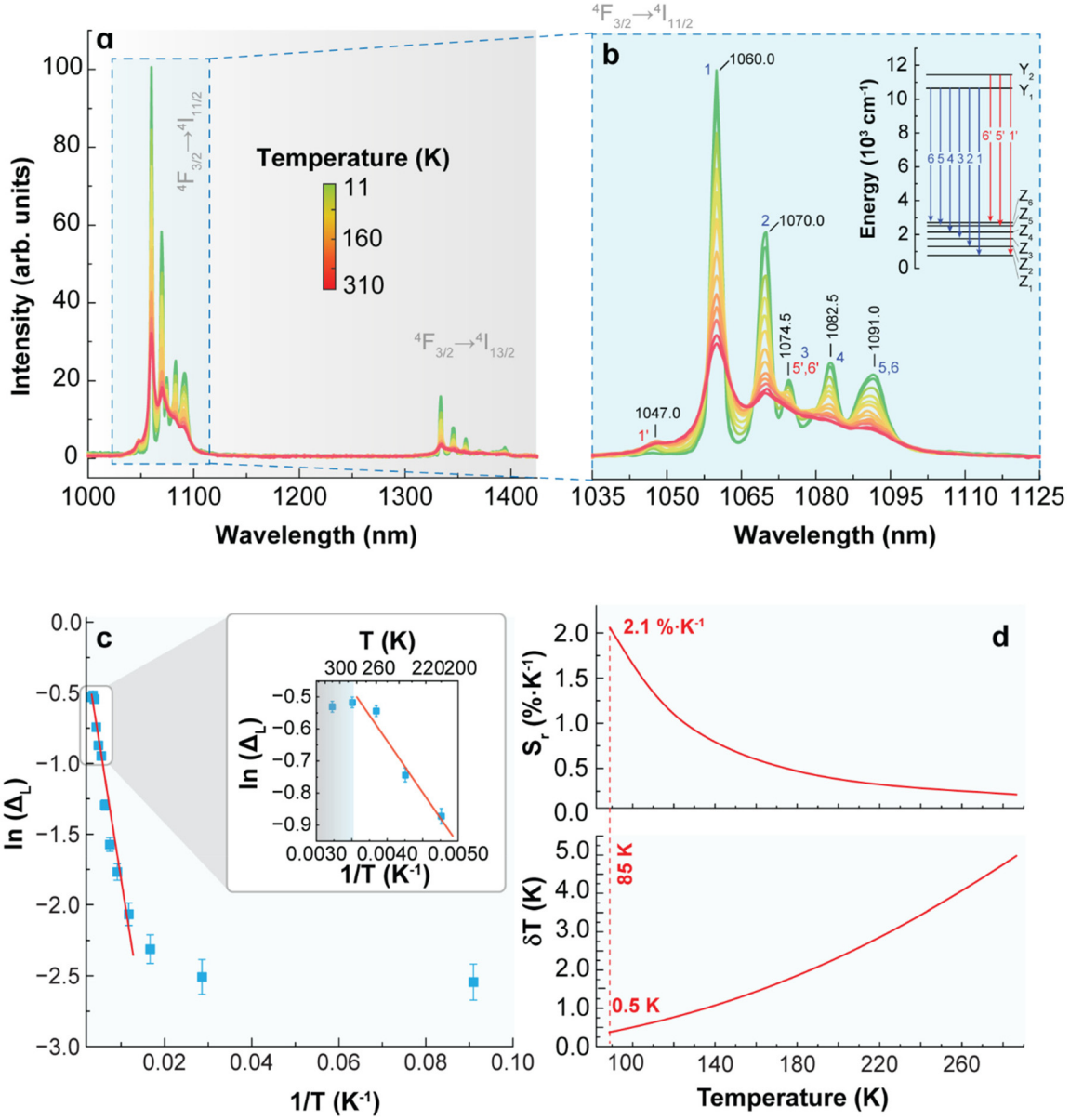

Fig. 4 (a) Temperature-dependent (11–310 K) emission spectra of **Nd_2** recorded under 370 nm excitation. (b) Enlarged view of the $^4F_{3/2} \rightarrow {}^4I_{11/2}$ transition highlighting its thermal evolution. The inset presents the corresponding energy-level diagram, indicating the Stark components and the assigned transitions. (c) Arrhenius plot of Δ_L as a function of 1/T. The line represents the best fit of the experimental data to $\Delta_L = B \exp\left(-\frac{\Delta E}{k_B T}\right)$ (r^2 > 0.900), where B is a fitting parameter and k_B the Boltzmann constant. The inset shows the magnification of the high-temperature region. The shadowed area marks the non-operative range. (d) Temperature dependence of S_r and δT values.

equilibrium between the Y_1 and Y_2 Stark components in this interval. The extracted energy gap, ΔE = 135 ± 13 cm^{-1}, agrees well with *ab initio* predictions and with the splitting estimated from the room-temperature emission spectrum (117–141 cm^{-1}, calculated from the energy differences between the 1047.0 (1′) and 1060.0 nm (1) bands, and between the 1074.5 (5′, 6′) and 1091.0 nm (5, 6) bands).

Under 370 nm excitation, a maximum relative sensitivity (S_m) of 2.1% K^{-1} and a minimum temperature uncertainty (δT) of 0.5 K are achieved at 85 K (Fig. 4d), highlighting the suitability of **Nd_2** as a single-center luminescent thermometer in the cryogenic regime. Notice, however, that for T > 285 K the thermometer is out of its operating range, as illustrated in the inset of Fig. 4c, precluding the application of **Nd_2** for near room-temperature sensing using Δ_L as the thermometric parameter.

The thermometric performance was also evaluated under direct excitation of the Nd^{3+} center at 804 nm. Since both the excitation wavelength and the NIR emission bands fall within BW-I and BW-II, measurements were conducted over the physiological temperature range (294–332 K) (Fig. 5a). The emission spectra show a general decrease in the intensities of the $^4F_{3/2} \rightarrow {}^4I_{9/2}$, $^4I_{11/2}$, $^4I_{13/2}$ transitions with increasing temperature. The Stark

splitting pattern of the $^4F_{3/2} \rightarrow {}^4I_{11/2}$ transition (Fig. 5b) closely resembles that observed under ligand-centered excitation. As previously established, the four peaks between 1059 and 1088 nm are dominated by Y_1-derived transitions, while the 1047.0 nm peak corresponds to the $Y_2 \rightarrow Z_1$ transition. Within the physiological temperature range, the Y_1-derived transitions decrease in intensity, whereas the 1047.0 nm band shows negligible temperature dependence (Fig. S6). This indicates that the Y_1 and Y_2 levels are already close to thermal equilibrium at these temperatures, and further heating does not significantly alter their relative populations, a tendency also observed under 370 nm at high temperature (inset of Fig. 4c). Consequently, the Boltzmann regime is no longer applicable in the 294–332 K interval. Instead, alternative temperature-dependent mechanisms, such as changes in radiative and non-radiative rates, phonon-assisted relaxation, or local-field effects, appear to dominate thermal evolution.

In the absence of a suitable physical model, an empirical second-degree polynomial function was therefore adopted for calibration within the 294–332 K interval (Fig. 5c). The thermometric parameter Δ_M was defined as the ratio between the integrated intensity of the four Y_1-derived peaks and that of the 1047.0 nm band corresponding to the $Y_2 \rightarrow Z_1$ transition. Within this temperature range and under 804 nm excitation, a maximum relative thermal sensitivity of S_m = 2.5% K^{-1} and a

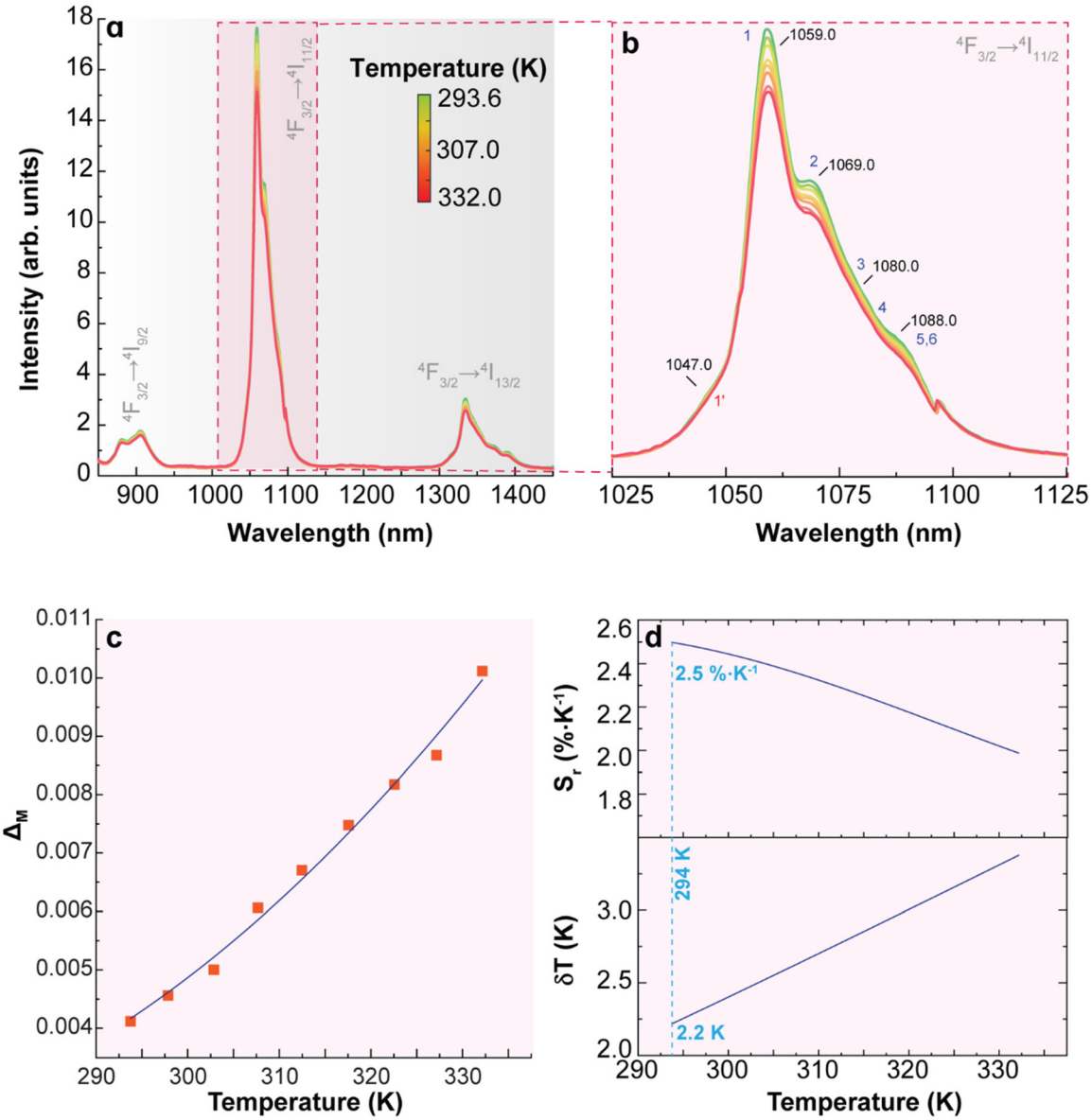

Fig. 5 (a) Emission spectra of Nd_2 recorded under 804 nm excitation at different temperatures. (b) Enlarged view of the temperature dependence of the $^4F_{3/2} \rightarrow {}^4I_{11/2}$ transition. The inset shows the corresponding energy level diagram detailing the Stark components and labelling the transitions. (c) Temperature dependence of Δ_M in the 293.6–332 K range. The line represents the best fit of the data to a 2nd degree polynomial ($r^2 > 0.999$). (d) Temperature dependence of S_r and δT values.

Table 1 Maximum relative thermal sensitivity (S_m) and minimum temperature uncertainty (δT) of reported Nd^{3+}-based coordination compounds upon ligand and metal-centered excitation and derived from LIR between different transitions or Stark components of a single transition

	Compound	λ/nm	Temperature range/K	Thermometric parameter		S_m/% K^{-1} (T/K)	δT/K (T/K)	Ref.
Ligand-centered excitation	{[Nd(acac)$_3$]$_2$(μ-bpm)} (**Nd$_2$**)	370	11–310	LIR (1060 nm Stark splitting)	$^4F_{3/2} \rightarrow {}^4I_{11/2}$ Stark components	2.1 (85)	0.5 (85)	This work
	[Nd_2^{III}(valdien)$_2$(acac)$_2$]	390	10–330	LIR (1045/1058)		0.3 (80)	0.1 (80)	25
	[Nd_2^{III}(valdien)$_2$(NO_3)$_2$]	390	10–330	LIR (1020/1105)		0.5 (40)	0.2 (40)	
	[Nd(TTA)$_3$(MeOH)$_2$]·0.5Azo-py	360	10–300	LIR (905/880)	$^4F_{3/2} \rightarrow {}^4I_{9/2}$ Stark components	<0.1 (125)	0.08 (125)	26
	[Nd(TTA)$_3$(MeOH)$_2$]·0.5Azo-py	392	75–300	LIR (905/880)		<0.1 (300)	0.02 (300)	
	[Nd (phen)$_3$(NCSe)$_3$]·0.3EtOH	364	150–300	LIR (895/874)		0.2 (170)	0.4 (300)	18
	[Nd(phen)$_3$(NCS)$_3$]·0.3EtOH	355	150–300	LIR (1060/874)	Two bands	0.2 (300)	0.4 (300)	
Metal-centered excitation	{[Nd(acac)$_3$]$_2$(μ-bpm)} (**Nd$_2$**)	804	294–332	LIR (1060 nm Stark splitting)	$^4F_{3/2} \rightarrow {}^4I_{11/2}$ Stark components	2.5 (294)	2.2 (294)	This work
	[(Nd(L))(μ-BTC)(H$_2$O)]$_6$·35H$_2$O	804	298–333	LIR (1065 nm Stark splitting)		2.4 (293)	—	24
	Nd-PDC	808	298–368	LIR (1065/1054)		0.36 (368)	0.08 (368)	23
	[NdL(CF_3SO_3)$_3$]	830	20–460	LIR (916/875)	$^4F_{3/2} \rightarrow {}^4I_{9/2}$ Stark components	0.5 (20)	—	27
	[(Nd(L)(NO_3))$_2$(μ-BDC)](NO_3)$_2$·H$_2$O	804	298–333	LIR (1065/1340)	Two bands	0.1 (293)	—	24

TTA: thenoyl(trifluoro)acetonate; Azo-py 4,4′-azopyridine; phen: 1,10-phenantroline; BTC: bencenetricarboxylate; BDC: bencenedicarboxylate; PDC = pyridine-3,5-dicarboxylate, L = 2*E*,6*E*,9*E*,13*E*-3,6,10,13-tetraaza-1,8(2,6)-dipyridina-cyclotetradecaphane-2,6,9,13-tetraene.

minimum temperature uncertainty of δT = 2.2 K are achieved at 294 K (Fig. 5d). Importantly, **Nd$_2$** maintains consistently high sensitivity across the entire physiological range (2.0–2.5% K^{-1}), underscoring its strong potential for biological temperature sensing.

For benchmarking purposes,[46] Table 1 gathers S_m and δT values of reported Nd^{3+}-based coordination compounds under both ligand and metal-centered excitation, derived from LIRs between different transitions or between Stark components of a single transition. The corresponding wavelengths used to define the thermometric parameters and operating temperature ranges are also included. To ensure meaningful comparison, systems are grouped according to the excitation pathway employed. In both categories, the S_m values obtained for **Nd$_2$** are the highest reported to date. Within the ligand-centered excitation group, other Nd-based dimers using the LIR between the Stark components of the $^4F_{3/2} \rightarrow {}^4I_{11/2}$ transition over comparable temperature ranges exhibit S_m values three to five times lower than that of **Nd$_2$**, highlighting its superior thermometric performance.

For metal-centered excitation, measurements have mainly been conducted within the physiological temperature range, reflecting the relevance of NIR-to-NIR emitters for biomedical applications. In this category, only the [(Nd(L))(μ-BTC)(H$_2$O)]$_6$·35H$_2$O[24] hexamer approaches the performance of **Nd$_2$**, with a slightly lower S_m value using the same Stark-component LIR method. All remaining compounds display sensitivities at least five times lower.

It is important to emphasize that δT depends not only on S_r but also on the signal-to-noise ratio.[46,47] Consequently, direct comparison of δT values obtained under different setups should be approached with caution. For compounds excited in the ligands and using Stark-component LIRs, δT values typically fall within the sub-Kelvin range, comparable to those obtained for **Nd$_2$**.[25] In contrast, δT is less systematically reported for compounds excited directly into the metal ions. Among the few available examples, the Nd–PDC complex exhibits a minimum δT of 0.08 K at 368 K,[23] lower than the 2.2 K obtained for **Nd$_2$** at 294 K. However, this comparison involves different estimation protocols: Nd–PDC accounts explicitly for detector characteristics,[48] whereas δT for **Nd$_2$** was initially calculated by standard error propagation (see SI). To enable a fair comparison, we recalculated δT for **Nd$_2$** using the same methodology applied to the Nd–PDC system, obtaining a minimum δT of 0.013 K at 294 K (Fig. S7). This demonstrates that, when evaluated using comparable criteria, the temperature resolution of **Nd$_2$** is of the same order of magnitude as the best-performing systems reported in the physiological temperature range. These results further emphasize the need for standardized procedures in estimating the thermometric figures of merit of luminescent thermometers.

Conclusions

Near-infrared luminescence of Nd^{3+} in the second biological window was demonstrated for **Nd$_2$** under both ligand-centered

excitation *via* the β-diketonate ($acac^-$) ligands and direct metal-centered excitation at 804 nm. The well-resolved Stark splitting observed at low temperatures, supported by *ab initio* calculations, enabled assignment of the Stark components involved in the $^4F_{3/2} \rightarrow {}^4I_{11/2}$ transition. Thermometry based on the luminescence intensity ratio (LIR) between these components yielded maximum relative thermal sensitivities of 2.1% K^{-1} at 85 K and 2.5% K^{-1} at 294 K under ligand- and metal-centered excitation, respectively, demonstrating excellent performance across both cryogenic and physiological regimes.

Compared with previously reported Nd-based coordination compounds, **Nd_2** exhibits among the highest sensitivities under both UV and NIR excitation. The sensitivity of 2.5% K^{-1} within the physiological temperature range underscores its strong potential for biomedical temperature sensing.

In addition to its high sensitivity, **Nd_2** offers operational flexibility through dual-excitation functionality, enabling adaptation to different experimental constraints such as penetration depth, background fluorescence, or excitation selectivity. These characteristics establish **Nd_2** as a versatile and tunable platform for NIR luminescent thermometry with relevance to advanced biological and photonic temperature-sensing applications.

Author contributions

Conceptualization: Y. G., P. F.; investigation and methodology: Y. G.; formal analysis: Y. G., J. C.-V., C. D. S. B., L. D. C., D. A., P. F.; data curation: D. A., P. F., J. C.-V., C. D. S. B., L. D. C., software: D. A.; resources: P. F., E. S., Y. G., R. C. S., D. A., L. D. C.; writing – original draft preparation: Y. G., writing – review & editing: Y. G., J. C.-V, L. D. C., C. D. S. B., P. F., E. S.

Conflicts of interest

There are no conflicts to declare.

Data availability

The data supporting this article have been included as part of the supplementary information (SI). Supplementary information is available. See DOI: **https://doi.org/10.1039/d5qi02484f**.

Acknowledgements

Y. G. thanks the financial support from the FONDECYT Postdoctoral Project 3220200. Y. G., P. F., E. S. and D. A thank Fondecyt Regular 1241928. D. A. thanks the FONDECYT Regular 1251041 project for financial support. Powered@NLHPC: this research was partially supported by the supercomputing infrastructure of the NLHPC (CCSS210001). This work was partially developed within the scope of the projects CICECO – Aveiro Institute of Materials, UIDB/50011/2020 (**https://doi.org/10.54499/UIDB/50011/2020**), UIDP/50011/2020 (**https://doi.org/10.54499/UIDP/50011/2020**) and LA/P/0006/2020 (**https://doi.org/10.54499/LA/P/0006/2020**) financed by Portuguese funds through the FCT/MEC (PIDDAC), and when appropriate, cofinanced by FEDER under the PT2020 Partnership through European Regional Development Fund (ERDF) in the frame of Operational Competitiveness and Internationalization Programme (POCI). This work was partially supported by Project PID2024-155748NB-I00, funded by MICIU/AEI/10.13039/501100011033 and by FEDER, EU. J. C.-V. thanks Xunta de Galicia for his postdoctoral fellowship (ED481D-2025/006). RCS acknowledges the financial support provided by projects CNPq (440225/2021-3), CAPES-AUGM 88881.004658/2024-01, and CNPq-FAPEG research fellowship (202510267001607).

References

1 J.-C. G. Bünzli and S. V. Eliseeva, Lanthanide NIR luminescence for telecommunications, bioanalyses and solar energy conversion, *J. Rare Earths*, 2010, **28**, 824–842.
2 G. Tessitore, G. A. Mandl, S. L. Maurizio, M. Kaur and J. A. Capobianco, The role of lanthanide luminescence in advancing technology, *RSC Adv.*, 2023, **13**, 17787–17811.
3 G. Neelima, K. Venkata Krishnaiah, N. Ravi, K. Suresh, K. Tyagarajan and T. Jayachandra Prasad, Investigation of optical and spectroscopic properties of neodymium doped oxyfluoro-titania-phosphate glasses for laser applications, *Scr. Mater.*, 2019, **162**, 246–250.
4 C. Chu, X. Yang, C. Li, C. Chen and S. Wang, Tunable quasi-three-level Nd:$NaLa(WO_4)_2$ laser pumped dual-wavelength Nd:$GdVO_4$/Nd:YVO_4 laser at 1341 and 1342 nm with adjustable ratio of output powers, *J. Opt.*, 2025, DOI: **10.1007/s12596-025-02482-4**.
5 B. J. Chen, L. F. Shen, E. Y. B. Pun and H. Lin, Nd^{3+}-doped ion-exchanged aluminum germanate glass channel waveguide, *Opt. Mater. Express*, 2015, **5**, 113.
6 S. Jin, R. Li, H. Huang, N. Jiang, J. Lin, S. Wang, Y. Zheng, X. Chen and D. Chen, Compact ultrabroadband light-emitting diodes based on lanthanide-doped lead-free double perovskites, *Light: Sci. Appl.*, 2022, **11**, 52.
7 M. Zhao, A. Sik, H. Zhang and F. Zhang, Tailored NIR-II Lanthanide Luminescent Nanocrystals for Improved Biomedical Application, *Adv. Opt. Mater.*, 2023, **11**, 2202039.
8 C. Alexander, Z. Guo, P. B. Glover, S. Faulkner and Z. Pikramenou, Luminescent Lanthanides in Biorelated Applications: From Molecules to Nanoparticles and Diagnostic Probes to Therapeutics, *Chem. Rev.*, 2025, **125**, 2269–2370.
9 X. Zhu, H. Zhang and F. Zhang, Expanding NIR-II Lanthanide Toolboxes for Improved Biomedical Imaging and Detection, *Acc. Mater. Res.*, 2023, **4**, 536–547.
10 H. Li, G. Bai, Y. Lian, Y. Li, L. Chen, J. Zhang and S. Xu, Advances in near-infrared-activated lanthanide-doped

optical nanomaterials: imaging, sensing, and therapy, *Mater. Des.*, 2023, **231**, 112036.
11 Y. Ning, M. Zhu and J. Zhang, Near-infrared (NIR) lanthanide molecular probes for bioimaging and biosensing, *Coord. Chem. Rev.*, 2019, **399**, 213028.
12 N. Jurga, M. Runowski and T. Grzyb, Lanthanide-based nanothermometers for bioapplications: excitation and temperature sensing in optical transparency windows, *J. Mater. Chem. C*, 2024, **12**, 12218–12248.
13 A. Puccini, N. Liu and E. Hemmer, Lanthanide-based nanomaterials for temperature sensing in the near-infrared spectral region: illuminating progress and challenges, *Nanoscale*, 2024, **16**, 10975–10993.
14 C. D. S. Brites, R. Marin, M. Suta, A. N. Carneiro Neto, E. Ximendes, D. Jaque and L. D. Carlos, Spotlight on Luminescence Thermometry: Basics, Challenges, and Cutting–Edge Applications, *Adv. Mater.*, 2023, **35**, 2302749.
15 E. Hemmer, A. Benayas, F. Légaré and F. Vetrone, Exploiting the biological windows: Current perspectives on fluorescent bioprobes emitting above 1000 nm, *Nanoscale Horiz.*, 2016, **1**, 168–184.
16 D. Qiu, P. Gutiérrez González, M. C. Iglesias de la Cruz, P. Molina, J. P Cascales, G. Lifante Pedrola, J. Marques-Hueso, S. Royuela, D. Jaque and J. Rubio Retama, Infrared emitting lanthanide doped nanoparticles provide sensing capabilities to coronary implants, *npj Nanophotonics*, 2025, **2**, 18.
17 M. Oggianu, V. Mameli, M. A. Hernández-Rodríguez, N. Monni, M. Souto, C. D. S. Brites, C. Cannas, F. Manna, F. Quochi, E. Cadoni, N. Masciocchi, A. N. Carneiro Neto, L. D. Carlos and M. L. Mercuri, Insights into NdIII to YbIII Energy Transfer and Its Implications in Luminescence Thermometry, *Chem. Mater.*, 2024, **36**, 3452–3463.
18 K. Kumar, O. Stefanczyk, K. Nakabayashi, Y. Mineo and S. I. Ohkoshi, Development of Nd(III)-Based Terahertz Absorbers Revealing Temperature Dependent Near-Infrared Luminescence, *Int. J. Mol. Sci.*, 2022, **23**, 6051.
19 M. Suta, Ż. Antić, V. Đorđević, S. Kuzman, M. D. Dramićanin and A. Meijerink, Making Nd^{3+} a sensitive luminescent thermometer for physiological temperatures—an account of pitfalls in boltzmann thermometry, *Nanomaterials*, 2020, **10**, 543.
20 L. Đačanin Far and M. D. Dramićanin, Luminescence Thermometry with Nanoparticles: A Review, *Nanomaterials*, 2023, **13**, 2904.
21 A. Nexha, J. J. Carvajal, M. C. Pujol, F. Díaz and M. Aguiló, Lanthanide doped luminescence nanothermometers in the biological windows: Strategies and applications, *Nanoscale*, 2021, **13**, 7913–7987.
22 M. A. Hernández-Rodríguez, A. D. Lozano-Gorrín, I. R. Martín, U. R. Rodríguez-Mendoza and V. Lavín, Comparison of the sensitivity as optical temperature sensor of nano-perovskite doped with Nd^{3+} ions in the first and second biological windows, *Sens. Actuators, B*, 2018, **255**, 970–976.
23 X. Zhou, Y. Wang, H. Wang, L. Xiang, Y. Yan, L. Li, G. Xiang, Y. Li, S. Jiang, X. Tang and X. Zhou, Nd^{3+} and Nd^{3+}/Yb^{3+}-incorporated complexes as optical thermometer working in the second biological window, *Sens. Biosensing Res.*, 2020, **29**, 100345–100354.
24 M. J. Maldonado, P. Farías-Carreño, Y. Gil, A. Vega, R. C. de Santana, D. Aravena, C. D. S. Brites, L. D. Carlos, A. N. C. Neto, F. Vetrone and P. Fuentealba, Anti-thermal quenching in NdIII molecular near-infrared thermometers operating at physiological temperatures, *Commun. Chem.*, 2025, **8**, 136.
25 A. G. Bispo-Jr, D. A. Gálico, R. M. Diaz-Rodriguez, J. S. Ovens, F. A. Sigoli and M. Murugesu, The role of terminal ligands in the slow relaxation of magnetisation and luminescence thermometry of dinuclear NdIII complexes, *Inorg. Chem. Front.*, 2023, **10**, 3929–3939.
26 K. Kumar, D. Abe, K. Komori-Orisaku, O. Stefańczyk, K. Nakabayashi, J. R. Shakirova, S. P. Tunik and S. I. Ohkoshi, Neodymium β-diketonate showing slow magnetic relaxation and acting as a ratiometric thermometer based on near-infrared emission, *RSC Adv.*, 2019, **9**, 23444–23449.
27 D. Marcinkowski, D. Prętka, P. Woźny, J. Kobylarczyk, A. Siwiak, D. Pakulski, V. Patroniak, K. Roszak, A. Katrusiak, R. Herchel, R. Podgajny, S. Sobczak, N. Majewska, S. Mahlik, M. Runowski and A. Gorczyński, Nd(III)-Based Temperature-Independent Manometer and Pressure-Independent Thermometer with Slow Relaxation of Magnetization, *Adv. Opt. Mater.*, 2025, **13**, 2500495.
28 Z. Huang, K. Li, Z. Zhang, J. Liu and D. Zhu, Sr_4GaNbO_8:Mn^{4+}: a novel perovskite-structured red-emitting phosphor for a luminescence lifetime thermometer with good relative sensitivity and repeatability, *J. Mater. Chem. C*, 2025, **13**, 4564–4575.
29 K. Li, Z. Huang and D. Zhu, Novel $Li_2Ga_{0.5}Sb_{0.5}O_3(Li_4GaSbO_6)$:$Mn^{4+}$ phosphors with multisite occupancy for efficient FIR and luminescence lifetime dual-mode thermometers, *Ceram. Int.*, 2025, **51**, 17433–17444.
30 C. D. S. Brites, P. P. Lima and L. D. Carlos, Tuning the sensitivity of Ln^{3+}-based luminescent molecular thermometers through ligand design, *J. Lumin.*, 2016, **169**, 497–502.
31 M. Wang, Y. Kitagawa and Y. Hasegawa, Current Development of Lanthanide Complexes for Biomedical Applications, *Chem. – Asian J.*, 2024, **19**, e202400038.
32 A. Yakubu, T. Suzuki and M. Kita, Homodinuclear lanthanoid(III) dithiocarbamato complexes bridged by 2,2′-bipyrimidine: Syntheses, structures and spectroscopic properties, *Polyhedron*, 2019, **171**, 515–522.
33 A. Bruker, *M. SAINTPLUS, V6.22*, Bruker AXS Inc., preprint.
34 G. M. Sheldrick, A short history of SHELX, *Acta Crystallogr., Sect. A: Found. Crystallogr.*, 2008, **64**, 112–122.
35 G. M. Sheldrick, Crystal structure refinement with SHELXL, *Acta Crystallogr., Sect. C: Struct. Chem.*, 2015, **71**, 3–8.
36 F. Neese, Software update: The ORCA program system—Version 5.0, *Wiley Interdiscip. Rev.: Comput. Mol. Sci.*, 2022, **12**, e1606.

37 F. Neese, The SHARK integral generation and digestion system, *J. Comput. Chem.*, 2023, **44**, 381–396.
38 P.-Å. Malmqvist and B. O. Roos, The CASSCF state interaction method, *Chem. Phys. Lett.*, 1989, **155**, 189–194.
39 D. Aravena, F. Neese and D. A. Pantazis, Improved Segmented All-Electron Relativistically Contracted Basis Sets for the Lanthanides, *J. Chem. Theory Comput.*, 2016, **12**, 1148–1156.
40 F. Weigend and R. Ahlrichs, Balanced basis sets of split valence, triple zeta valence and quadruple zeta valence quality for H to Rn: Design and assessment of accuracy, *Phys. Chem. Chem. Phys.*, 2005, **7**, 3297.
41 M. Reiher, Douglas-Kroll-Hess theory: A relativistic electrons-only theory for chemistry, *Theor. Chem. Acc.*, 2006, **116**, 241–252.
42 Y. Gil, M. J. Maldonado, R. C. de Santana, A. Vega, P. Fuentealba and D. Aravena, Improvement of electronic structure calculations for the interpretation of the emission spectrum for NdIII complexes, *Phys. Chem. Chem. Phys.*, 2025, **27**, 9847–9854.
43 N. Marino, D. Armentano, G. De Munno, F. Lloret, J. Cano and M. Julve, Towards a better understanding of honeycomb alternating magnetic networks, *Dalton Trans.*, 2015, **44**, 11040–11051.
44 R. Ilmi and K. Iftikhar, Synthesis, visible light absorption and luminescence of bipyrimidine bridged dinuclear lanthanide complexes of 2,4-pantanedione, *Inorg. Chem. Commun.*, 2010, **13**, 1552–1557.
45 G. Zucchi, O. Maury, P. Thuéry and M. Ephritikhine, Structural diversity in neodymium bipyrimidine compounds with near infrared luminescence: From mono- and binuclear complexes to metal-organic frameworks, *Inorg. Chem.*, 2008, **47**, 10398–10406.
46 C. D. S. Brites, S. Balabhadra and L. D. Carlos, Lanthanide-Based Thermometers: At the Cutting-Edge of Luminescence Thermometry, *Adv. Opt. Mater.*, 2019, **7**, 1801239.
47 T. P. van Swieten, A. Meijerink and F. T. Rabouw, Impact of Noise and Background on Measurement Uncertainties in Luminescence Thermometry, *ACS Photonics*, 2022, **9**, 1366–1374.
48 C. D. S. Brites, A. Millán and L. D. Carlos, in *Handbook on the Physics and Chemistry of Rare Earths*, Elsevier B.V., 2016, vol. 49, pp. 339–427.

